

# LeakyTrack: Non-Coherent Single-Antenna Nodal and Environmental Mobility Tracking with a Leaky-Wave Antenna

Yasaman Ghasempour  
Rice University  
ghasempour@rice.edu

Chia-Yi Yeh  
Rice University  
cy20@rice.edu

Rabi Shrestha  
Brown University  
rabi\_shrestha@brown.edu

Yasith Amarasinghe  
Brown University  
yasith\_amarasinghe@brown.edu

Daniel Mittleman  
Brown University  
daniel\_mittleman@brown.edu

Edward W. Knightly  
Rice University  
knightly@rice.edu

## ABSTRACT

Radio frequency signals have the potential to convey rich information about a node’s motion and surroundings. Unfortunately, extracting such information is challenging, previously requiring accurate phase measurement, large antenna array structures, or extensive training. In this paper, we present *LeakyTrack*, a novel system that enables non-coherent and training-free motion sensing with a single antenna. The key idea is to create unique spectrally coded signals at different spatial directions so that geometric properties of the receiving node, as well as any potential objects in the environment, leave spectral footprints on the collected signal. To do so, we exploit a THz leaky-wave antenna and realize a *color-coded scan* in which signals with distinct spectral characteristics simultaneously emit across the angular domain. *LeakyTrack* infers nodal and environmental motion by analyzing the received spectral profile. We evaluate the performance of *LeakyTrack* via extensive over-the-air experiments.

## CCS CONCEPTS

• **Computer systems organization** → **Embedded and cyber-physical systems.**

## KEYWORDS

Wireless Sensing, Terahertz Waves, Leaky-Wave Antenna

### ACM Reference Format:

Yasaman Ghasempour, Chia-Yi Yeh, Rabi Shrestha, Yasith Amarasinghe, Daniel Mittleman, and Edward W. Knightly. 2020. *LeakyTrack: Non-Coherent Single-Antenna Nodal and Environmental Mobility Tracking with a Leaky-Wave Antenna*. In *The 18th ACM Conference on Embedded Networked Sensor Systems (SenSys '20)*, November 16–19, 2020, Virtual Event, Japan. ACM, New York, NY, USA, 13 pages. <https://doi.org/10.1145/3384419.3430717>

Permission to make digital or hard copies of all or part of this work for personal or classroom use is granted without fee provided that copies are not made or distributed for profit or commercial advantage and that copies bear this notice and the full citation on the first page. Copyrights for components of this work owned by others than ACM must be honored. Abstracting with credit is permitted. To copy otherwise, or republish, to post on servers or to redistribute to lists, requires prior specific permission and/or a fee. Request permissions from [permissions@acm.org](mailto:permissions@acm.org).

*SenSys '20, November 16–19, 2020, Virtual Event, Japan*

© 2020 Association for Computing Machinery.

ACM ISBN 978-1-4503-7590-0/20/11...\$15.00

<https://doi.org/10.1145/3384419.3430717>

## 1 INTRODUCTION

Radio frequency (RF) sensing employs the fundamental principle that changes in the characteristics of electromagnetic (EM) waves as they travel in the wireless medium can provide rich information about a receiver’s properties (such as distance, velocity, shape, size, and orientation) as well as the objects that have interacted with the waves on their route. It is typically viewed that such properties (i) cannot be inferred with a single antenna, as a single antenna provides only one spatial observation point; and (ii) cannot be inferred solely based on detecting incident power, but rather require careful timing analysis of the phase of the incoming signal, i.e., coherent reception.

In this paper, we for the first time, show that neither of these common beliefs are true. In particular, we present the design and experimental evaluation of *LeakyTrack*, a novel non-coherent and training-free system that identifies nodal and environmental motion using a single antenna. Our key idea is to divide the region around a sensing node into a virtual canvas of segments and to assign a unique color code to each segment. If these segments were to be painted based on their color codes, the sensing module can discover a target’s location based on its color. We propose a similar concept of “*painting by numbers*” in which the number represents a wavenumber (or equivalently frequency). In particular, we create a unique spectral code in each direction and develop a method to correlate spatial information with spectral properties, i.e., to map the canvas to colors. Our key contributions are as follows:

First, we transmit unique spectral codes in the spatial domain by introducing a novel RF sensing architecture in which the transmitter (TX) and receiver (RX) are equipped with a Leaky-Wave Antenna (LWA). A LWA is a passive device that allows a traveling wave inside a waveguide to leak into free-space with the key property that the emission angle from the waveguide is coupled to the frequency of the input signal [7]. We exploit this property and develop the first LWA-based nodal and environmental sensing system. While a naive LWA implementation would create a spectral code at each direction by varying the frequency of the input signal (i.e., painting one segment at a time), we instead show how to simultaneously scan a wide range of spatial angles (i.e., painting the entire canvas at once) by injecting a time-domain terahertz (THz) pulse, or equivalently a broadband signal in frequency domain, into the LWA. Consequently, different frequency components are decomposed and emerge at different directions, thus filling the entire angular space with signals that have unique spectral content or color, which we also refer to as a color-coded scan.

Second, we demonstrate how LeakyTrack senses nodal and environmental mobility by analyzing the spectral profile of the collected signals. In particular, we first devise a model that allows a LWA-equipped receiving node to locally predict its angular location and orientation relative to the TX. Since we deliberately discriminate transmissions of different frequencies in the spatial domain, the RX only captures certain signals with unique spectral codes. We show that the location-specific spectral codes experience a further non-uniform and frequency-dependent loss at the RX LWA related to the RX's orientation. LeakyTrack leverages these insights to jointly extract location and orientation from the spectral information that was harvested rapidly, via a single pulse of broadband emission. In addition to tracking device motion, we characterize the impact of environmental objects on the color-coded signals. Intuitively, the presence of an object in the wireless medium can obstruct the reception of certain signals. Analogous to the shadow of an object in a painted canvas that affects only certain colors, in a color-coded scan, the object is unlikely to attenuate all emitted frequencies evenly. Instead, it imposes a partial and frequency-selective distortion according to its geometric properties. LeakyTrack identifies such features, including the object's angular location and size, by measuring the object's spectral footprints.

Finally, we implement the key components of LeakyTrack and perform extensive over-the-air experiments in various settings. Our testbed consists of a THz pulse generator, a broadband receiver, and custom LWAs configured in numerous topologies including with obstructing objects. Our key findings are as follows:

(i) We experimentally realize a color-coded scan by injecting a THz pulse into a LWA and measuring the emitted spectral-spatial profiles in different directions. We demonstrate that LeakyTrack can successfully sense and track the RX's parameters, even in complex real-world trajectories, with average estimation error of  $< 1^\circ$  for angular position and  $< 2^\circ$  for rotation angle.

(ii) We find that such motion inferences are feasible only within certain regimes. We characterize these detection zones, considering the physical limitation of our single-antenna architecture and the inherent spectral behavior of the color-coded scan. We discover that LeakyTrack is prone to higher errors in regimes where spectrum is a slow-varying or irregular function of angle. Further, rotating a device causes power attenuation due to frequency misalignment, which ultimately yields negligible spectral information being received such that spatial inferences cannot be made. Nonetheless, we show that a surprisingly large range of rotation angles can be accurately tracked.

(iii) We measure the frequency-selective blockage footprints of objects at different locations and sizes. Within the field-of-view of the color-coded scan, we find that LeakyTrack accurately estimates the object's geometric properties such as spatial position and size. A relatively larger object leaves more pronounced spectral footprints making the detection easier; nonetheless, under full blockage, the object positioning would be ambiguous.

(iv) We experimentally explore the tradeoff between estimation accuracy, airtime overhead, and computation complexity and quantify how improved computational efficiency costs lower estimation accuracy or higher airtime channel use.

## 2 RELATED WORK

Radio frequency (RF) spectrum has been very attractive as a sensing modality for interactive systems as RF sensors, unlike vision-based techniques, are unaffected by lighting or atmospheric conditions and better preserve privacy. RF-based sensing has been explored extensively in the literature. Unfortunately, achieving high sensing resolution often demands complex system architectures; namely, large antenna arrays, coherent wideband transceivers, and extensive training or calibration.

**Multi-Antenna RF Sensing.** Multi-antenna radio systems have been exploited in the literature to sense Received Signal Strength (RSS) and Angle of Arrival (AOA) to infer the motion of a radio-equipped node (a.k.a. active sensing) or an object (a.k.a. passive sensing) [8, 30, 39]. The sensing resolution, however, is limited by the number of antennas in the systems. Other works emulate multiple receiving or transmitting antennas by creating a synthetic aperture based on the movement of the active or passive target [2]. Even though such solutions eliminate the need for large arrays, they restrict the type of motion that can be detected. More recently, mmWave devices allow for miniaturized phased-array antennas to create highly directional beams. Scanning the space by steering such directional beams can automatically correlate the relative positioning of an RF source (transmitter or an object reflecting RF signals) with RX's location through the beam direction in-use [37]. Instead, we propose a *single-antenna* architecture that is capable of sensing objects and tracking any arbitrary motion of a receiver.

**Coherent Wideband Solutions.** Another body of work exploits Time of Flight (ToF) measurements or phase variations at coherent transceivers for RF sensing [1]. It is important to note that the spatial resolution of such systems is a function of the total bandwidth of the transmitted waveform and depending on the utilized bandwidth the ranging accuracy can vary from a couple of meters to few centimeters. Hence, using mmWave and Terahertz frequencies, with a large swath of available spectrum, is inherently more advantageous. Yet, the key challenge is that extracting ToF or phase information requires tight synchronization between nodes, which becomes increasingly challenging in higher frequencies. Furthermore, due to extremely higher attenuation, received signals can have low SNR, demanding expensive low-noise electronics to extract phase reliably [34].

Instead, in LeakyTrack, we adopt a *noncoherent* approach that relies solely on the relative power over different frequency sub-channels to infer nodal or environmental motions. This relaxation simplifies the sensing architecture, eliminates the need to keep tight synchronization between the transmitter and receiver, and is robust to small-scale channel variations.

**Training Based RF Sensing.** Other works adopt training techniques such that the recognition system uses a classifier that is trained and tested under a similar environmental conditions in which it will be deployed. These solutions follow the general architecture of machine learning-based classification systems that are tailored for a specific sensing purpose, e.g., human presence detection [2], fall detection [29, 36], activity recognition [6, 22], and localization [32, 42]. Depending on the technology in-use and the training set size, tracking small-scale motions with even

sub-millimeter accuracy has been demonstrated for gesture sensing applications [24]. The training phase, however, may be computationally demanding and time-consuming, especially since detection accuracy or ability to discriminate fine-grained target pattern is typically a function of the training set size [10].

Instead, LeakyTrack requires *no training* and no pre-computation. In particular, we introduce an explicit model that correlates the nodal and environmental movements to the received spectral properties that are independent of the environment. Furthermore, LeakyTrack not only classifies the type of activity (e.g., type of motion), but it also estimates the amount of that activity (e.g., the amount of receiver rotation or changes in an object location).

**Visible Light Sensing.** A popular non-RF solution is visible light localization and tracking. Typically, multiple existing indoor luminaries are used to achieve sub-meter accuracy with multi-lateration [23, 40]. Other works use non-linear intensity differences between two sensors to estimate AOA and localize using fingerprinting with 3+ light sources of known location [43] or unknown positions [18]. Another related approach is to use cameras to capture images of distinguishable LED lamps and localize using image processing techniques [13, 21]. Another recent trend in light-based systems is to localize digitally to guarantee high resilience against random noise [25, 38]. Finally, in LiDAR ranging systems, the target is illuminated with laser light and differences in laser return times are used for distance inference. The disadvantages of visible light sensing are rooted in reflectivity limitations of light pulses causing vulnerability to ambient light and inability to track passive objects, especially when combined with nodal motion. Camera-based solutions require much higher power and computational resources. Further, LiDAR uses high-power lasers imposing eye-safety concerns.

**Leaky Wave Antennas.** Having been used in the RF region since at least the 1940s, LWAs have a long history [7]. LWAs have been studied mainly as a potential candidate for THz networks since they offer a low-profile and flexible solution for the challenging problem of beam steering in the THz regime [3, 4, 12, 19, 33, 34]. Specifically, LWAs allows for controlling the beam steering direction by tuning the transmit frequencies [17, 28]. Other work explored the capacity and limitations of these antennas in multiplexing [20, 26], terahertz radar [5, 27], link discovery [14, 15], and physical-layer security [41]. In contrast, in this work, we present the first-ever use of the LWA as a physical medium for non-coherent RF sensing.

### 3 SYSTEM ARCHITECTURE

In this section, we explain the background of leaky-wave antennas and present our sensing architecture.

#### 3.1 Primer on Leaky-Wave Antennas

A leaky-wave antenna can be realized by two metal plates placed in parallel with open sides. By cutting a slot in one of the plates, we allow guided waves to “leak” energy into free-space, or to receive energy from free-space. We can treat the leaky waveguide slot as a finite-length aperture, which produces a diffraction pattern in the far-field. For a diffracting aperture (i.e., slot length) of  $L$  and the dominant  $TE_1$  mode, the far-field radiation electric field  $E$  can be

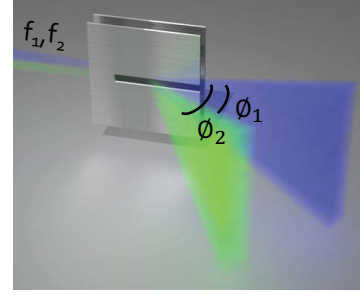


**Figure 1: Two waves injected to the leaky-wave antenna leak at different angles such that high-frequency wave (blue) emits at lower angle compared to the low-frequency wave (green), i.e.,  $f_1 > f_2$  results in  $\phi_1 < \phi_2$ .**

derived as [16, 35]

$$E(f, \phi) \propto \text{sinc} \left( [\beta(f) - j\alpha + k_0 \cos \phi] \frac{L}{2} \right), \quad (1)$$

where  $\text{sinc}(x) = \sin x/x$ ,  $\alpha$  is a parameter that describes the loss of energy in the guided mode due to leakage out of the slot,  $k_0$  is the free-space wave vector number (i.e.,  $k_0 = \frac{2\pi f}{c}$  in which  $c$  is the speed of light and  $f$  represents frequency), and  $\phi$  is the propagation angle of the free-space wave relative to the waveguide’s propagation axis (so that  $\phi = 0$  corresponds to the emission in parallel to the LWA’s plates).

In the above equation,  $\beta(f)$  is the frequency-dependent propagation constant of guided waves. For the parallel-plate waveguide, the dominant transverse electric (TE) mode is  $TE_1$  mode, and the propagation constant  $\beta$  of the  $TE_1$  mode is

$$\beta(f) = k_0 \sqrt{1 - \left( \frac{c}{2bf} \right)^2}, \quad (2)$$

where  $b$  represents the distance between the two metal plates of the waveguide.

**Frequency-dependent radiation in LWAs.** Based on the radiation pattern described in Eq. (1), the energy emitted at a particular angle is coupled with the frequency of input waves. The radiation function  $E(f, \phi)$  maximizes when  $\text{Re} \left\{ (\beta(f) - j\alpha - k_0 \cos \phi) \frac{L}{2} \right\} = 0$ . Because of the frequency dependence of propagation constant  $\beta(f)$ , this condition results in a coupling between frequency and emission angle from the slot, given by

$$\phi = \sin^{-1} \left( \frac{c}{2bf} \right) \quad (3)$$

Eq. (3) suggests that the larger the input frequency, the lower the max-power emission angle from the slot. Fig. 1 depicts a LWA device with two injected frequencies shown in blue ( $f_1$ ) and green ( $f_2$ ) such that  $f_1 > f_2$ . We observe that the green-colored wave emits at a larger angle compared to the blue-colored wave.

#### 3.2 Sensing Architecture

We leverage the frequency-dependent radiations in LWAs for enabling the nodal and environmental sensing functionality. We equip wireless transmitter and receiver with a single LWA device. We emphasize that LWA structures can easily meet the power, size, weight, and cost considerations of future handheld devices since

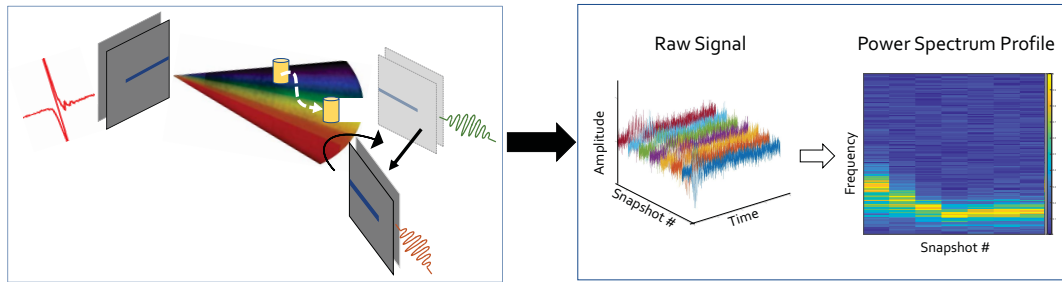


Figure 2: LeakyTrack design overview for passive and active sensing.

they are passive, light (< 3 oz), and cheap (< \$10). We also envision the capability of generating and detecting broadband signals (up to 1 THz) or equivalently the ability to sweep through different frequencies at wireless nodes.

In transmission mode, the injected signal to the LWA leaks out and creates directional radiation whose characteristics (i.e., main-lobe direction) depends on the frequency of that signal. In reception mode, the impinging waves are coupled into the waveguide and then guided toward the broadband receiver located at the end of the metal plates. The RX signal depends on the TX and RX movement, as well as the potential object in the environment. Therefore, we assume a fixed TX and aim to infer changes in the environment or RX’s geometric properties by exploring the spectral features of the received signal. To this end, LeakyTrack relies solely on power measurements across a range of frequencies and does not require timing or phase information.

Note that emissions from the LWA span in 3D space, as also shown in Fig. 1, such that a signal emits narrowly in azimuth (horizontal) but broadly in elevation (vertical). In principle, we can develop mathematical models that allow nodal and environmental sensing based on the 3D spatial-spectral codes. Yet, for simplicity, we focus on 2D sensing, because unless two different receivers are stacked on top of each other, 2D sensing is sufficient to distinguish between receivers at different azimuth angles. We leave the 3D expansion of LeakyTrack for future endeavors.

## 4 LEAKYTRACK DESIGN

In this section, we describe the design components of LeakyTrack that leverages the spatial-spectral coupling in LWA radiation patterns to enable a color-coded scan and infer the spatial locations of LWA-equipped RXs as well as LWA-free objects.

### 4.1 Design Overview

LeakyTrack is the first non-coherent single-antenna sensing system that can sense nodal and environmental motion using a LWA. We leverage the antenna’s inherent frequency-dependent radiation to deliberately discriminate the spread of different frequencies in the angular space so that the spatial information correlates with the spectral properties of the received signals. We introduce a color-coded scan to simultaneously cover a wide spatial domain in a single transmission. LeakyTrack then extracts the geometric properties of a RX (e.g., location and orientation) and the passive objects (e.g., location and size) based on their spectral footprints on the received power spectrum profile. This can potentially

enable many applications including accurate indoor localization and tracking, object and human presence detection, and efficient coordination of directional wireless networks via fast mobility adaptation and blockage recovery.

The fundamental design principles of LeakyTrack are illustrated in Fig. 2. We inject a time-domain terahertz pulse (equivalently a broadband signal) into the LWA. Different frequency components will decouple and emerge at different directions forming a color-coded scan as shown in Fig. 2. At the RX, a portion of these EM waves arrive having spectral characteristic that depend on objects in the wireless medium and the RX’s geometric properties. The EM waves ultimately impinging on the RX’s LWA couple into the waveguide through the open slot, travel inside the waveguide, and are measured at the plate ends.

The LeakyTrack architecture can be used to infer the motion of both the RX itself as well as the potential environmental object. Sensing a LWA-equipped device (a.k.a. active sensing), we show how to model the spectrum as a function of the device’s spatial location and orientation relative to the TX’s waveguide. The presence of objects within the field-of-view of our color-coded scan obstructs the reception of certain EM waves and yields a frequency-selective blockage. We show how this partial blockage relates to the object’s geometric properties (e.g., position and size). Note that we are referring to the objects that are partial obstruction of a Line-Of-Sight (LOS) path since with a full blockage, no signal is measured, and consequently, no spatial information is conveyed. Therefore, LeakyTrack senses a static or moving object (a.k.a. passive sensing) via measuring its spectral footprints (see Fig. 2).

Finally, LeakyTrack achieves the best of two worlds: the high-resolution in wide-band RF sensing and low-complexity in the architecture of non-coherent and single-antenna systems. In particular, unlike conventional wide-band techniques that require complex architectures due to the need for tight synchronization, LeakyTrack simplifies the sensing architecture by relying solely on the power or RSS measurements. On the other side, LeakyTrack overcomes the shortcomings of RSS-based single-antenna schemes by simultaneously transmitting waves with unique spectral signatures in different directions. Next, we illustrate the mathematical model that enables the nodal motion sensing and the object sensing without a training phase.

### 4.2 Modeling Spatial-Spectral Footprints

We consider a static transmitter that creates frequency-dependent radiation patterns by passing a THz pulse through a LWA. We first

isolate and model the received spectrum as a function RX's angular position. Then, for a fixed RX placement, we explore the impact of RX rotation on the spectral profile. Finally, we introduce an optimization framework that extracts nodal motion by comparing the modeled spectral profile against the measured spectrum.

**4.2.1 Spectral Contribution of RX's Location.** To relate the received spectral properties to the device's location, the first step is to model the frequency-dependent directional radiations in LWAs. LeakyTrack enables a color-coded scan by injecting a THz pulse (which contains a wide range of frequencies up to 1 THz) into the TX's waveguide. The LWA acts as a directional antenna emitting waves into the free-space; albeit, with a spatial bias such that the main lobe direction is a nonlinear function of the frequency. We denote  $D(f, \phi)$  as the directivity gain of frequency  $f$  defined as the radiant intensity that a LWA creates in a particular direction  $\phi$  against the average value over all directions:

$$D(f, \phi) = \frac{|E(f, \phi)|}{\frac{2}{\pi} \int_0^{\frac{\pi}{2}} |E(f, \phi)| d\phi}, \quad (4)$$

where  $E(f, \phi)$  is the far-field electric field pattern in Eq. (1) and the denominator represents the average radiated intensity over  $[0, \frac{\pi}{2}]$ .

The emitted signals from the waveguide subsequently traverse in the wireless medium and impinge on RX's LWA. Even though such emissions happen simultaneously in all directions within a sector of  $90^\circ$ <sup>1</sup>, only those signals with sufficient directivity gain along the RX's LOS direction can be received.

Hence, we model  $r_{im}(f)$ , the impinging power over any given frequency, as follows:

$$r_{im}(f) \propto P_{tx}(f) D(f, \phi_D) \left(\frac{c}{4\pi df}\right)^2, \quad (5)$$

where  $\phi_D$  represents the LOS angle between the two nodes,  $P_{tx}(f)$  is the transmit power budget for each frequency, and  $c$  is the free-space speed of light. The term  $\left(\frac{c}{4\pi df}\right)^2$  describes the free-space Friis propagation loss. Fig. 3 demonstrates an example scenario with frequency-dependent radiation patterns depicted in different colors. Translation of a mobile device would change the relative TX-RX angular positioning (i.e.,  $\phi_D$ ); hence, rendering impinging waves with distinct spectral properties.

**Interference of Background Reflection.** We consider a LOS channel model due to the sparse scattering at frequencies above 100 GHz [31]. In particular, the likelihood of multipath interference is low due to the high reflection attenuation (e.g., every bounce off of an object costs 10 dB [19]). Nonetheless, it is worth noting that signals may still suffer from distortion under background reflection. Such reflections, if they exist, would have different departure angles compared to the LOS path. Hence, the spectral content of a non-LOS (NLOS) path would be different from the LOS's spectral characteristics provided there is sufficient angular separation between the two paths. Hence, one can devise strategies to identify and isolate the LOS spectral band for RF sensing with LeakyTrack. However, we limit the scope of this paper to LOS channels and leave the exploration of NLOS scenarios for future work.

<sup>1</sup>The angular range can be increased to  $360^\circ$  by extending the node architecture, for instance by employing a multi-face LWA structure. However, exploring such solutions is beyond the scope of this paper.

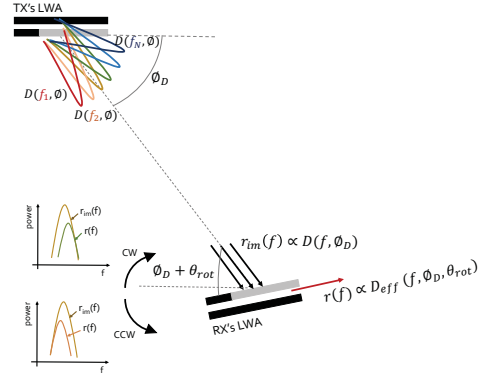


**Figure 3: Nodal motion tracking by creating frequency-dependent radiation patterns and processing the spectral characteristics of the received waveform.**

**4.2.2 Spectral Contribution of RX's Orientation.** Finally, the impinging waves are coupled into the RX LWA and guided toward the broadband detector. Intuitively, if the RX's LWA is parallel to the TX's LWA, then the air-to-waveguide coupling loss is negligible, and we expect similar spectral characteristics for coupled and impinging waves. However, when the incident angle is different from  $\phi_D$ , then the coupled waves would experience a mismatch loss. In principle, the LWA has a reciprocal radiation pattern; thus, when operated as a receiver, free-space waves with frequency  $f$  would couple best into the waveguide if they arrive at the slot with the angle given by Eq. (3). The amount of coupling mismatch loss depends on the discrepancy between the correct angle (for each frequency  $f$ ) and the incident angle.

We denote  $\theta_{rot}$  as the RX's rotation angle compared to perfect alignment with the TX's LWA. In other words,  $\theta_{rot}$  is the difference between the angle of incidence and departure. We assume a reciprocal frequency-dependent reception pattern as defined in Eq. (4). Hence, we can model the composite impact of TX and RX spatially-biased LWA filters as  $D(f, \phi_D) \times D(f, \phi_D + \theta_{rot})$ . Nonetheless, LWAs are passive devices and cannot amplify signals. Therefore, the power of the coupled waves for any given frequency cannot be larger than the impinging power. We account for this physics-driven requirement by bounding the effective directivity to the original transmit directivity:

$$D_{eff}(f, \phi_D, \theta_{rot}) = \min \left( D(f, \phi_D) D(f, \phi_D + \theta_{rot}), D(f, \phi_D) \right), \quad (6)$$

where  $D_{eff}(f, \phi_D, \theta_{rot})$  characterizes the effective end-to-end directivity gain at any frequency. Note that  $\theta_{rot}$  can be a positive or negative scalar, depending on the RX's orientation. If the incident angle is far from the angle of departure (i.e., large  $\theta_{rot}$ ), one would expect that the RX receives no signal. However, our analysis reveals that LeakyTrack can support a fairly large  $\theta_{rot}$  without complete loss of signal (see Sec. 6).

**Rotation Direction.** Although all frequency components would encounter some coupling loss on the waveguide interface, this attenuation is non-uniform across different sub-channels and depends on the rotation direction. Fig. 3 shows the power spectrum of impinging and coupled waves for clockwise (CW) and counter-clockwise (CCW) rotations.

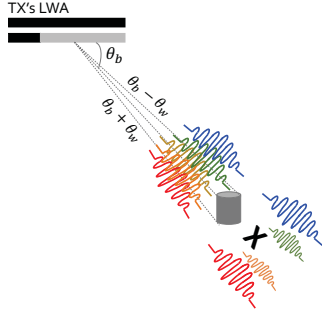


**Figure 4: Object tracking based on the frequency-selective distortion imposed by the object's spatial footprints.**

CW rotation of RX's LWA (negative  $\theta_{rot}$ ) makes the angle of incidence smaller than the optimum angle. Recall from Sec. 3 that the angle of emission (here reception) is inversely and non-linearly proportional to the frequency. Hence, with smaller incident angles, higher-frequency tones within the spectral band of the impinging waves are better coupled into the waveguide, whereas lower tones suffer from increased coupling mismatch loss.

Conversely, with CCW rotation (positive  $\theta_{rot}$ ), the increase in the angle of incidence yields a relatively better coupling for low-frequency components while imposing higher loss on high-frequency components of the impinging waves. Fig. 3 demonstrates an example scenario in which the spectral band of coupled waves differs from the that of impinging waves depending on the direction of rotation. In LeakyTrack, we take hints from these insights to extract the amount and the direction of rotation.

**4.2.3 Integrating Nodal Parameters.** Since the RX's spatial location and orientation both contribute to the spectral properties of the received waveform, we can write the received power for a given frequency  $f$ , LOS angle  $\phi_D$ , and rotation angle  $\theta_{rot}$  as follows:

$$r(f, \phi_D, \theta_{rot}) \propto P_{tx}(f) D_{eff}(f, \phi_D, \theta_{rot}) \left(\frac{c}{4\pi d f}\right)^2 \quad (7)$$

Note that the first-order spectral attributes are embedded in the effective directivity pattern  $D_{eff}(f, \phi_D, \theta_{rot})$ . First, recall that  $P_{tx}$  is a scalar representing the transmit power. Second, we assume that the distance  $d$  is slowly changing such that the amount of spectral change induced by Friis path loss is not significant between two consecutive inferences. Nonetheless, as different frequencies experience different propagation attenuations, this opens up the possibility to harness this distance-dependent loss for ranging and proximity estimation, which is a subject of our future work.

**4.2.4 Frequency-Selective Blockage.** The emitted EM waves suffer from penetration loss when encountering an object on their route toward the receiver. In a color-coded scan, the scattering object is unlikely to attenuate all frequency components evenly. Instead, the object induces a partial and frequency-selective distortion according to its geometric features. Fig. 4 depicts a scattering object located at angle  $\theta_b$  relative to the transmitter. The object's spatial footprint imposes a spectral distortion on the waves emerging in directions of  $\theta_b \pm \theta_w$  in which  $\theta_w$  denotes the half-angle size of the object in the angular regime.

We model the spectral distortion due to the presence of an object located at center angle  $\theta_b$  (w.r.t the TX) with half-angle size of  $\theta_w$  as follows:

$$B_{ndx}(f, \theta_b, \theta_w) = \frac{\int_{\theta_b - \theta_w}^{\theta_b + \theta_w} D(f, \phi) d\phi}{\int_0^{\frac{\pi}{2}} D(f, \phi) d\phi}, \quad (8)$$

where  $B_{ndx}$  represents blockage index and  $D(f, \phi)$  is the directivity gain as defined in Eq. (4). When  $\theta_w = 0$ , no object exits between the TX and RX and the blockage index  $B_{ndx} = 0$ . Maximum blockage occurs when the center of the object is located at  $\phi_f$  (i.e., the max-power emission angle). Note that  $\theta_w$  is the projected size of an object from TX's point of view, such that  $\theta_w$  of a big object that is far from the TX may be similar to the half-angle size of a smaller object closer to the TX.

### 4.3 Motion Detection and Tracking

While Eq. (7) models the expected relative power spectrum based on RX geometric properties, we can also measure the actual received power spectrum at the RX. We envision a periodic color-coded scan to track the nodal and environmental motion by measuring the spectral variations. In practice, power measurements are available over a discrete set of frequencies depending on the clock sampling rate. We denote  $r_{msr}(f)$  as the power measurement for any frequency  $f$  within the available set of frequencies. Therefore, we estimate the geometric parameters of the RX as well as any potential objects via the non-linear least squares optimization framework below that minimizes the distance between measured data and our model after proper scaling:

$$\begin{aligned} \phi_D^*, \theta_{rot}^*, \theta_b^*, \theta_w^* = \\ \arg \min_{\phi_D, \theta_{rot}, \theta_b, \theta_w} \sum_f |r_{msr}(f) - r(f, \phi_D, \theta_{rot})(1 - B_{ndx}(f, \theta_b, \theta_w))|^2, \end{aligned} \quad (9)$$

where  $\phi_D^*$  is the LOS departure angle estimate and  $\theta_{rot}^*$  is the estimated rotation angle relative to the perfect waveguide alignment.  $\theta_b^*$  and  $\theta_w^*$  capture the object's spatial placement and size. Moreover, the summation is over the discrete range of frequencies supported by the broadband detector. We emphasize that no phase information is used in this methodology; thus, LeakyTrack is a non-coherent scheme. Note that environmental mobility (i.e., movement of an object) manifests as changes in  $\theta_b^*$  in consecutive measurements. Similarly, nodal motion can be inferred from LOS or rotation angle variations.

**Tradeoff between Airtime Overhead and Computational Complexity.** Finding a global minimum for the non-linear least squares problem in Eq. (9) would require a brute-force search over a discrete set of values for the variables of interest (namely,  $\phi_D$ ,  $\theta_{rot}$ ,  $\theta_b$ , and  $\theta_w$ ). The computational complexity of such an exhaustive search relates to the search space size such that the number of iterations is on the order of  $N^4$  when each variable tries  $N$  values.

Alternatively, we can solve this non-linear least squares problem via computationally efficient algorithms such as Gauss-Newton and Davidon-Fletcher-Powell. Nonetheless, these algorithms are sensitive to the initial parameter estimates since inaccurate initialization (that is far from the optimum values) can yield ill-conditioning, divergence, or landing on a local minimum

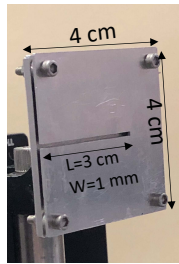


Figure 5: The custom LWA used in our measurement setup.

rather than a global minimum. To avoid stale initial estimates, we need to increase the tracking rate, meaning the number of pulse transmissions per unit time, rendering higher airtime overhead and channel use. Therefore, we study the tradeoff between computational complexity and airtime overhead in Sec. 6.3.

## 5 EXPERIMENTAL PLATFORM

To evaluate the performance of LeakyTrack, we conduct extensive over-the-air experiments. The key components of our measurement setup are the THz pulse emitter, broadband detector, and our custom-built LWA. For THz pulse generation and detection, we use the T-Ray 4000 TD-THz system [11]. The interchangeable fiber-coupled sensor heads deliver a picosecond duration time-domain THz pulse or equivalently a broadband waveform in the frequency-domain that ranges up to 1 THz. On the receiver side, with the sampling rate of 12.8 THz (1 sample every 78 femtoseconds), we can observe frequencies up to 6.4 THz with a resolution of 3.13 GHz. We build a custom LWA device that consists of two  $4 \times 4 \text{ cm}^2$  metal plates with a thickness of 1 mm, as shown in Fig. 5. We put the plates in parallel with 1 mm separation and create a slot on one plate with 3 cm length and 1 mm width to allow guided waves to leak into free space. Note that the slot length should be at least an order of magnitude larger than the plate separation to allow the energy leak out along the aperture as waves propagate inside the waveguide. Slot length and plate separation impact the spatial-spectral properties of the color-coded scan and such dependencies are captured in Eq. (1)-(3).

Fig. 6 demonstrates our measurement setup for nodal sensing. Our broadband source generates THz pulses which are focused to the LWA via a lens with a focal distance of 6 cm. The composing frequencies then decouple and emit at different directions realizing

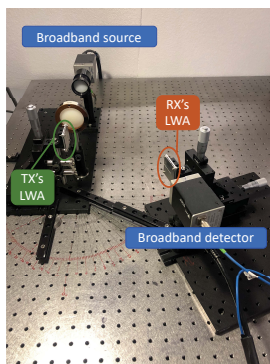


Figure 6: Our experimental setup for active sensing.

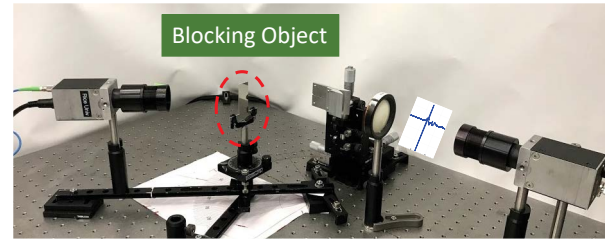


Figure 7: Our experimental setup for passive object sensing.

a color-coded scan. The RX's LWA and the broadband detector are mounted on a rotating arm that facilitates different LOS and orientation configurations.

Fig. 7 depicts our experimental setup for passive object detection and tracking. Reflection and absorption coefficients of an object vary depending on frequency and the material's properties. Yet, exploring the absorption and scattering behavior of different materials in sub-THz bands is beyond the scope of this paper. Here, as a proof-of-concept analysis, we use objects made from aluminum sheets in multiple sizes.

Due to hardware limitations of the low-power THz source, we are bound to conduct experiments in small scales (up to a meter). In particular, our THz source emits an average power of roughly  $-10 \text{ dBm}$ , which is the time-averaged power, integrating over the entire (1 THz) spectral band. Hence, the power in 1 kHz bandwidth is  $-100 \text{ dBm}$ . Scaling up the transmitter-receiver distance could be achieved by increasing the power of the transmitter. For example, prior work reported a CMOS-based widely tunable source that achieves about  $-10 \text{ dBm}$  in 1 kHz bandwidth, over the entire range 100 – 300 GHz offering a factor of  $10^9$  increase in output power compared to our THz source [9]. Exploring the details of such CMOS-based technologies (e.g., power efficiency) is beyond the scope of this paper. Note that the LWA is itself a passive device and increasing the transmit power does not affect the spatial-spectral patterns nor the design of LeakyTrack. Further, time-domain measurements are translated to power spectrum via a 4096-point FFT, which are then directly used as input to the LeakyTrack. Hence, LeakyTrack does not require any pre-processing techniques and it is not computationally demanding.

## 6 EVALUATION

In this section, we evaluate the key components of LeakyTrack via over-the-air experiments.

### 6.1 Nodal Motion Sensing

We explore the capability of LeakyTrack in nodal motion sensing for three types of mobility: (i) *Translational Mobility*: in which the RX's position changes while keeping the same orientation; (ii) *Rotational Mobility*: in which the RX has a fixed location but varying orientation; and (iii) *Concurrent Translation and Rotation*: where we consider real-world motions with a mixture of both translation and rotation.

**6.1.1 Translational Mobility.** We first experimentally investigate the performance of LeakyTrack in detecting and tracking translational motion.

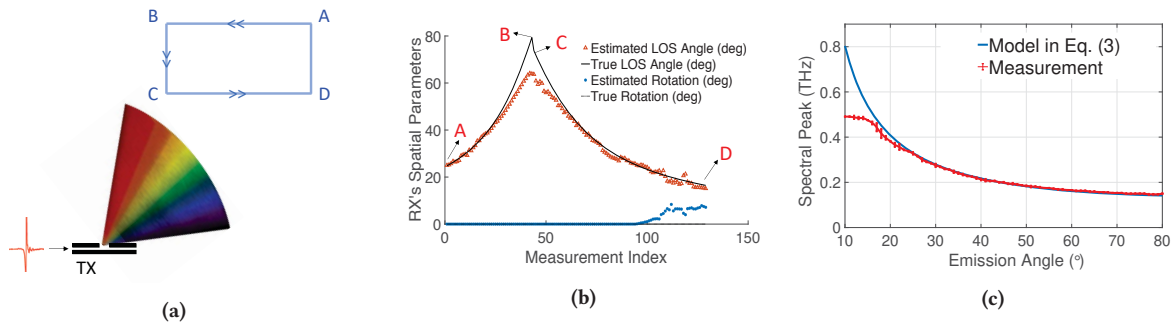


**Figure 8: Translational mobility experiment: (a) the schematic of measurement setup, (b) Nodal motion parameters estimated by LeakyTrack, (c) the angle-frequency coupling in LWAs, theory vs. experiment.**

**Setup.** We study a fixed LWA-equipped TX and a mobile RX. Fig. 8a depicts our experimental setup in which the TX conducts a color-coded scan by injecting a pulse into its LWA. The RX travels along the trajectory  $A \rightarrow B \rightarrow C \rightarrow D$  while measuring the received power spectrum. To isolate the spectral variation due to translation, we mandate continued alignment between the RX and TX waveguides (i.e.,  $\theta_{rot}$  is zero). We use each measured signal independently and as stand-alone data to extract nodal motion parameters. In other words, our inference scheme does not include the history of previous measurement instances here.

Fig. 8b presents the motion parameter estimates (including LOS and rotation angles) achieved by LeakyTrack against the ground truth. We observe that LeakyTrack accurately infers the LOS angle for a range of angles. In particular, Fig. 8b reveals that the LOS angle (i.e.,  $\phi_D$ ) estimates deviate from ground truth for angles above  $60^\circ$ . Moreover, LeakyTrack mistakenly detects rotation when the RX approaches point D in the trajectory (equivalently,  $\phi_D$  getting below  $18^\circ$  in the angular domain).

To understand the reasons behind these imperfections, we measure the spectral characteristics of radiations as a function of emission angle and compare it with the model from Sec. 3. Fig. 8c plots the peak frequency of measured power spectrum vs. receiver's angle for a range of  $10^\circ$  to  $80^\circ$  degrees with a resolution of  $1^\circ$ . In the same plot, we show the theoretical spectral peak from Eq. (3). The results show good agreement between the model and measurement data for angles above  $20^\circ$ . When  $\phi_D$  is below  $20^\circ$ , the corresponding peak frequencies are above 400 GHz and those components are fundamentally weaker, due to the spectrum of the illumination source used in our measurements. Hence, when exposed to coupling loss, the signal level degrades to the noise level yielding an increased measurement error. Additionally, Eq. (3) does not account for non-idealities in the waveguide geometry such as finite non-zero plate thickness that contributes to a more complex spectrum. These effects are likely to become more pronounced at small angles, where the effective propagation length inside the leaky-wave slot is larger.

Moreover, as shown in Fig. 8c, for angles above  $55^\circ$ , the peak frequency is a relatively flat (or slowly varying) function of the emission angle. This means that radiation at those emission angles are expected to have similar spectral characteristics making it difficult for LeakyTrack to extract the correct angle. Besides, the spectral resolution of any real-world broadband receiver is finite and bound to its clock sampling rate. The frequency resolution

in our setup is 3.1 GHz; thus, a small spectral shift may cause an estimation error of several degrees in this regime.

*Findings: LeakyTrack can successfully extract the RX's spatial position by conducting a color-coded scan and assessing the spectral profile of received signals. Yet, LeakyTrack is prone to estimation errors at regimes where spectrum is a slowly varying or irregular function of emission angle.*

**6.1.2 Rotational Mobility.** Here, we first experimentally explore how spectral properties vary as a function of RX rotation. Then, we analyze the capability of LeakyTrack in inferring the amount of rotation in different settings. To this end, we consider a fixed LOS configuration with path angle  $\phi_D = 30^\circ$  and rotate the RX's LWA such that angle of incident changes in steps of  $2^\circ$  in both CW and CCW directions. At each rotation setting, we collect raw data from the broadband detector located at one end of the waveguide.

We find that total RX power is maximum when the receiving waveguide is perfectly aligned with the transmitting waveguide. Any other orientation configuration imposes a power attenuation due to the coupling mismatch loss. Interestingly, Fig. 9 reveals that the attenuation is non-uniform across the spectrum. Specifically, for any CW rotation, the lower half of the band faces a relatively higher attenuation compared to higher frequency components. Since the effective impinging angle decreases (see Fig. 3), the antenna frequency-dependent directivity shifts toward higher frequencies, i.e., positively biasing higher tones while weakening lower ones. As shown in Fig. 9a, the extent of weakening worsens with larger rotation angles.

Similarly, Fig. 9b demonstrates that CCW rotation introduces non-uniform frequency-dependent loss by moving the directivity

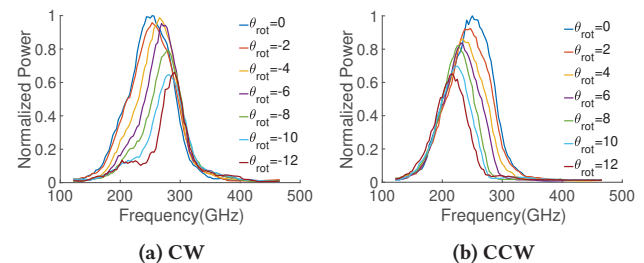


**Figure 9: The power spectrum of the received signals with different RX's rotation configurations.**

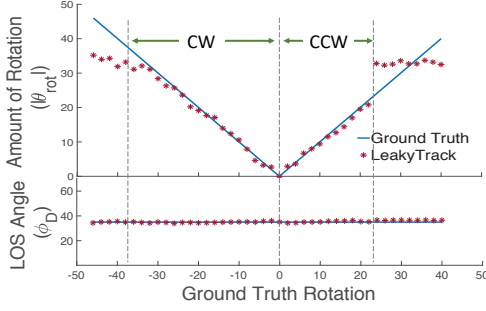


**Figure 10: LeakyTrack rotation estimation for a range of CW and CCW rotation angles at fixed LOS angle of 37 degrees.**

pattern of the RX’s LWA toward lower frequencies. Nonetheless, LWA is a passive device and cannot amplify the signal; thus, the coupled waves’ power at any frequency cannot be more than that of impinging waves. These measurement insights were the building block for LeakyTrack’s rotation inference illustrated in Sec. 4.

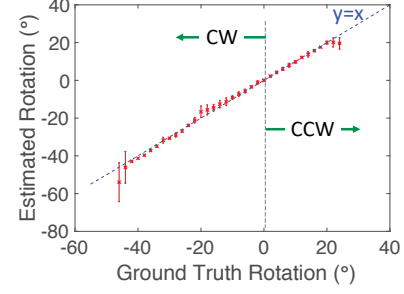
Next, we analyze the performance of LeakyTrack in estimating nodal rotation in fixed LOS configurations. We exploit the same setup, but this time, we locate the RX’s LWA along with the broadband detector at different angular positions such that  $\phi_D$  adopts a discrete choice of angles from  $25^\circ$  to  $65^\circ$ .

Fig. 10 presents the nodal motion estimates against the amount of true rotation when the geometric angle between the TX and RX waveguides is  $37^\circ$ . We observe that LeakyTrack can successfully track RX rotation for a range of CW and CCW rotations (shown within dashed lines) while consistently extracting the correct and fixed LOS angle. Beyond this detection range (which we also call detection zone), however, the estimates deviate from the ground truth. Obviously, if the rotation angle is too large, then the received spectral information becomes close to the noise level, and the rotation angle cannot be correctly detected. Note that the maximum measurable rotation is asymmetric with respect to the direction of rotation. We further characterize the detection zone below.

Finally, Fig. 11 summarizes LeakyTrack’s performance in rotation tracking. By compiling all measurements at a given rotation angle (at each  $\phi_D$ ), we extract the measurement uncertainty in the rotation angle as a function of the true degree of rotation. The figure depicts the average extracted rotation angle at many values of  $\phi_D$  along with error bars to indicate standard deviation. The uncertainty increases somewhat for larger rotations since a smaller signal is measured. Nevertheless, over the range of accessible rotation angles, the average estimation error is less than  $1.5^\circ$ .

*Findings: We experimentally showed how the spectral characteristics of impinging waves change with LWA orientation. LeakyTrack leverages these spectral inferences and accurately estimates the rotation angle and direction of a LWA-equipped node.*

**6.1.3 Detection Zone.** The results in Fig. 8b and Fig. 10 suggest that device motion inference is feasible only within certain regimes. In principle, LeakyTrack can conduct a color-coded scan over a range of  $90^\circ$  as signal leakage falls within a sector of  $90^\circ$ . However, as discussed above, these emissions are relatively less well-behaved close to  $0^\circ$ . To overcome this physics-driven limitation, we can extend the sensing architecture. For instance, although we excite



**Figure 11: The overall rotation estimation accuracy of LeakyTrack.**

the transmitter’s LWA in a single-sided configuration, it would be possible to excite the device from both sides, thus doubling the accessible angular by producing a symmetric emission pattern at angles  $90^\circ < \phi_D < 180^\circ$ . Further, a more complicated waveguide slot geometry could be employed to cover a larger range of angles. Yet, exploring such architectures is beyond the scope of this paper.

The rotation detection zone is somewhat different since rotation, unlike translation, can cause severe power attenuation. Obviously, if the rotation angle is too large, then no spectral information is received, and the rotation angle cannot be detected. Yet, predicting the maximum sensible value of  $\theta_{rot}$  for any given RX location  $\phi_D$  is not straightforward.

Let us denote  $\gamma_{th}$  as the power detection threshold that should be set based on the noise statistics. We can define the spectral edges of a received signal as follows:

$$\begin{aligned} f_{min} &= \arg \min_f D_{eff}(\phi_D, \theta_{rot}, f) > \gamma_{th}, \\ f_{max} &= \arg \max_f D_{eff}(\phi_D, \theta_{rot}, f) > \gamma_{th}, \end{aligned} \quad (10)$$

where  $f_{min}$  and  $f_{max}$  are the minimum and maximum spectral tone whose power is above  $\gamma_{th}$ . Clearly, perfect alignment ( $\theta_{rot} = 0$ ) yields the maximum received spectral band ( $f_{max} - f_{min}$ ). However, this band shrinks with device rotation either by decreasing  $f_{max}$  under CCW rotation or increasing  $f_{min}$  under CW rotation. If the spectral band of the coupled signal gets to zero, the received spectral profile would not carry any meaningful information and thus rotation detection becomes infeasible. Hence, we define the detection zone as the maximum rotation angle that provides non-zero spectral band (i.e.,  $f_{max} > f_{min}$ ).

Fig. 12 shows the range of detectable rotations as a function of RX angular placement. We observe, for a surprisingly large range of angles which depends on  $\phi_D$ , rotation can be tracked. The reason is that the impinging waves contain a wide range of frequencies at any emission angle. For certain RX locations, the detection zone is dominated by physical considerations. For instance, for  $\phi_D < 32^\circ$ , the maximum CW rotation is bound to  $\theta_{rot} > -\phi_D$ . Beyond this limit, the effective incident angle becomes negative meaning the impinging waves would hit the opposite plate. Similarly, for  $\phi > 65^\circ$ , the maximum CCW rotation is limited to  $\theta_{rot} < 90 - \phi_D$ . Even though waves with incident angles higher than  $90^\circ$  would still couple into the waveguide, they propagate on the opposite direction inside the waveguide; hence, we cannot measure such signals unless we place a second detector at the opposite end of the waveguide.

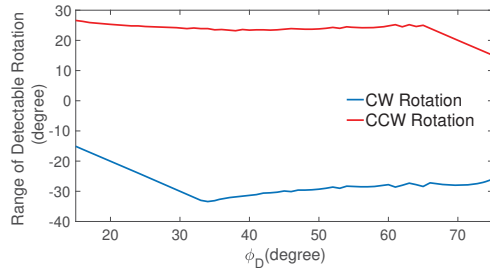


Figure 12: Range of detectable at different RX locations.

Moreover, Fig. 12 reveals that CW rotation offers a relatively wider detectable range compared to CCW. This can also be observed in Fig. 10. The reason is lower frequencies are more resilient toward coupling mismatch loss. In other words, a fixed amount of CCW rotation renders higher loss on large frequency components ( $f_{max}$ ) compared to the loss on lower frequencies ( $f_{min}$ ) caused by the same amount of CW rotation.

*Findings: As the misalignment between transmitting and receiving LWAs increases, ultimately, no signal gets coupled in and no spectral inference can be made. Nonetheless, a large range of rotation angles can be accurately tracked.*

**6.1.4 Concurrent Translation and Rotation.** In real-world systems, devices can traverse complex trajectories in which both translation and rotation are combined. Hence, we aim to characterize the performance of LeakyTrack in such nodal mobility scenarios. Due to hardware limitations, realizing continuous motion in our experiments is not possible. Therefore, we emulate continuous motion by discretizing the space of movement, and each time we configure the RX at the pre-selected location and orientation before collecting the measurement data.

**Setup.** We consider a pseudo-random trajectory in which  $\phi_D$  varies between  $25^\circ$  to  $65^\circ$  in steps of  $5^\circ$  and the rotation angle takes multiples of  $2^\circ$  on both CW and CCW directions (e.g.,  $\pm 2, \pm 4, \pm 6$ , etc.) as long as it falls within the detection zone described in Sec. 6.1.3. Initially, the RX chooses a random  $\phi_D$  and rotation angle from the above sets. Subsequently, at each measurement snapshot, the RX can jump into a different position and orientation provided that it stays within the acceptable regions. Note that this trajectory does not mandate a constant translation/rotation speed as the amount of movement between consecutive measurements might vary. We run LeakyTrack on the collected trace to infer the nodal motion parameters. We emphasize that LeakyTrack’s estimation at each snapshot is a stand-alone function of the power spectrum measured at that instance, independent of other previous instances.

Fig. 13 plots the nodal motion parameters and the geometric true values in an example pseudo-random trajectory. In this experiment, the angular placement of the RX and its orientation both contribute to the received spectral profile. Nonetheless, the parameters estimated by LeakyTrack accurately follow the ground truth values. Note that the rotation angles are reported with respect to perfect alignment with the TX’s LWA. Of course, one can easily find the amount of rotation between subsequent measurements.

*Findings: We demonstrate that LeakyTrack can sense complex nodal mobility patterns that include combined rotation and translation with high accuracy.*

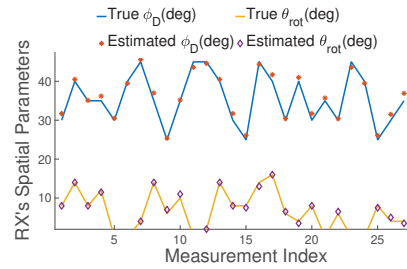


Figure 13: Concurrent translation and rotation estimation by LeakyTrack in a pseudo-random trajectory.

## 6.2 Environmental Sensing

**Setup.** Fig. 14 shows the schematic of our measurement setup. The receiver is placed facing the LWA slot at a distance of 25.4 cm from the LWA and has a lens with a diameter of 4 cm. We move an aluminum object from right to left with steps of 2 mm such that the object trajectory is perpendicular to the LWA-RX axis. For each object placement, we inject a THz pulse to the waveguide and measure the received spectrum. We can find a geometric Field of View (FoV) for any given configuration, as shown in the figure. In principle, an object can only impact the received spectral profile when located within the FoV. Further, we mark the angle at which the object first touches the FoV as the *right edge (RE)* and the angle at which the object leaves the FoV as the *left edge (LE)*.

**6.2.1 Exploring Frequency-Selective Object Footprints.** To experimentally explore an object’s spectral footprints, we deploy the setup in Fig. 14 and place the RX at the angle of  $35^\circ$ . Fig. 15a presents the measured power heatmap over different frequencies as a function of the object’s location ( $\theta_b$ ). For each  $(f, \theta_b)$  element, we normalize the corresponding power to the maximum received power over the entire angular and spectral range. This heatmap includes the frequency range of 150 GHz to 500 GHz with a resolution of 3.1 GHz.

The yellow high-power region (power values close to 1) corresponds to the object placed outside of the FoV; hence, the spectral distortion is negligible. This region spans over 245 to 285 GHz with maximum power at 265 GHz which also follows the expected spectral peak from Eq. (3). When the object angle approaches  $35^\circ$  from RE, the power corresponding to the second-half of the spectrum (265 – 285 GHz) drops faster. This is because, due to the angle-frequency coupling in LWA, the object blocks the waves that contain mostly higher tones. As expected, the overall power loss is maximum when the object is located at

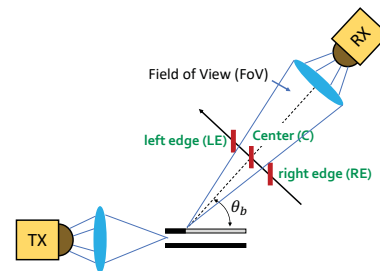
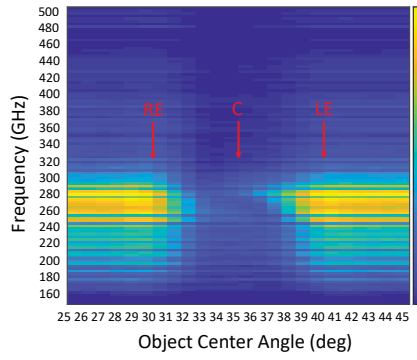
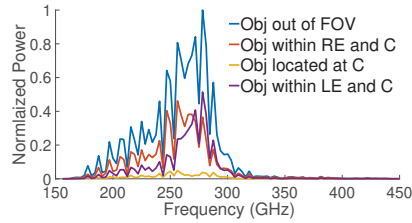


Figure 14: The schematic of object sensing experiments.



(a) Power heatmap



(b) Power spectrum for 4 different object locations

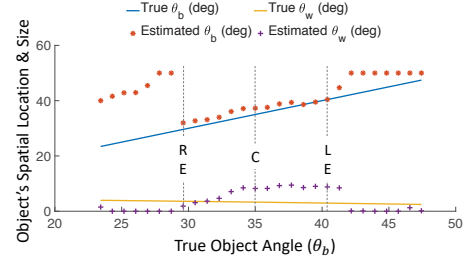
**Figure 15: Experimental exploration of frequency-selective spectral variations due to an object in the wireless medium.**

the center of the FoV. As  $\theta_b$  shifts to larger angles, the power at high-frequency components recovers relatively faster. Finally, the object's spectral footprint gets negligible as it leaves the FoV.

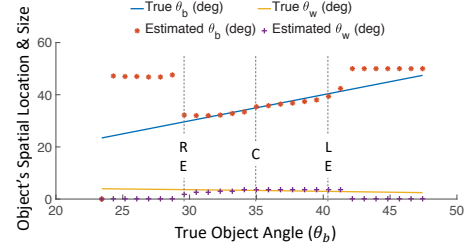
Next, using the same setup, we study the spectral profile of four regions: outside the FoV, between RE and C, exactly at C, and between LE and C. Fig. 15b plots the normalized power spectrum corresponding to these regions. The frequency-dependent power distortion is again observable here. For such a small object in-use, one might expect a narrow spectral footprint that involves sudden power reduction over a small set of frequencies while other components remain intact. But interestingly, Fig. 15b reveals that the reduction spreads over a wide range of frequencies, albeit, non-uniformly. The reason is mainly rooted in the radiation properties of our color-coded scan in which each frequency radiates not only at the maximum-power radiation angle, but also over a range of angles surrounding it. LeakyTrack leverages such non-uniform spectral footprints for object detection and tracking.

*Findings: An object leaves spectral footprints since it obstructs the reception of EM waves whose emission directions are correlated with their spectral content. We experimentally characterized how this partial blockage relates to the object's position.*

**6.2.2 Object Tracking with LeakyTrack.** For evaluating the sensing accuracy of LeakyTrack, we consider the same setup as shown in Fig. 14. We place the RX at  $35^\circ$  and move the object on a rail perpendicular to the LWA-RX line. We define  $\theta_w$  as the angular representation of the object size. Fig. 16a shows the object parameters estimates ( $\theta_b$  and  $\theta_w$ ) as a function of the true object angle. We also mark the RE, C and LE points on the same plot. We observe that, when the object is inside the FoV, the estimated  $\theta_b$  is in good agreement with the true object angle. However, this does not hold true for the estimation of  $\theta_w$ .



(a)



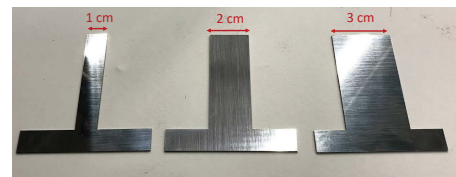
(b)

**Figure 16: LeakyTrack object tracking (a) before  $\alpha$  optimization, (b) after  $\alpha$  optimization.**

The reason behind the imprecise estimation of  $\theta_w$  in LeakyTrack is rooted in Eq. (8). According to this model,  $\theta_w$  controls the spectral width of the object-induced distortion such that larger  $\theta_w$  translates to a wider affected band. Obviously,  $\theta_w = 0$  means no object was identified. However, there is another parameter embedded in  $D(f, \phi)$  that also affects the spectral width. As defined in Eq. (1),  $\alpha$  accounts for the attenuation of the guided waves and determines the angular spread of each frequency component emerging from the waveguide: larger  $\alpha$  corresponds to a wider spread and vice versa. In principle, there is no simple analytical model for  $\alpha$ ; yet, for a fixed node architecture (i.e., a given LWA geometry), it is a deterministic function of frequency that can be measured and known a priori. Hence, we measure  $\alpha$  values and incorporate them into our model. Fig. 16b confirms the improved performance of LeakyTrack after optimizing  $\alpha$ .

*Findings: LeakyTrack exploits the non-linear frequency-selective blockage induced by an object to accurately estimate its geometric properties such as spatial position and size.*

**6.2.3 Object Size.** One key factor that determines the extent of the spectral footprint is the object's size. To investigate this factor, we repeat our experiments with three different sized objects as shown in Fig. 17. Fig. 18 shows the heatmap of the measured power spectrum as a function of the object's spatial location for these three objects.


**Figure 17: Deploying objects in different sizes into the experimental setup.**

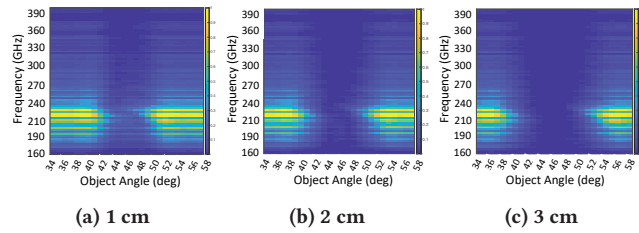


**Figure 18: The power spectrum heatmap vs. object location for different object sizes.**

As expected, a larger object tends to occlude a wider set of frequencies. Further, we observe that the full blockage (dark blue) region expands as the object’s size increases. In such scenarios, LeakyTrack can easily detect the presence of a blocking object; yet, the position of the object would be ambiguous.

On the other extreme, a very small object yields an insignificant spectral change that might get dissolved in the irregularities of the frequency-dependent radiations or the existing channel noise. Note that the absolute size of the object is irrelevant. Instead, the spectral footprint is determined by the angular width of the object which itself depends on the object’s orientation and distance to the TX. However, the results in Fig. 16 show that LeakyTrack can successfully extract  $\theta_w$  without knowing distance or orientation.

*Findings: Larger objects leave more pronounced spectral footprints that makes detection easier; nonetheless, under full blockage, the object positioning would be ambiguous.*

### 6.3 Trading Airtime Overhead for Computational Complexity

So far, we used a brute-force search mechanism in LeakyTrack, in which the search space increases with the granularity of the parameters of interest. In this approach, we estimated the nodal or environmental motion parameters for each measurement instance without using any information from previous instances. Here, alternatively, we implement a less computationally demanding scheme that leverages the past inferences. We envision periodic THz pulse excitation (every  $T$  seconds) so that the receiver updates its motion estimates by assessing the received power spectrum profile. At each measurement instance, we solve the non-linear least squares problem in Eq. (9) using the Gauss-Newton algorithm such that the estimates from the previous measurement are adopted as the initial guess.

We emphasize that inaccurate initialization (that is far from the optimum values) can yield ill-conditioning, divergence, or landing into a local minimum rather than a global minimum. Obviously, a faster tracking rate (i.e., smaller  $T$ ) offers a better initialization status, yet costs higher time overhead and channel use. In particular, since broadband pulse transmissions occupy the entire spectral band, data transmissions in the close vicinity of a sensing node need to be stopped or might otherwise experience interference. Moreover, the speed of mobility (e.g., translation or rotation velocity) also affects the staleness of the initial guess: faster speed causes higher changes in the motion parameters between two consecutive measurements separated by  $T$ . Instead of evaluating these two factors separately, we consider the amount of change in the RX’s spatial position during one cycle  $T$ .

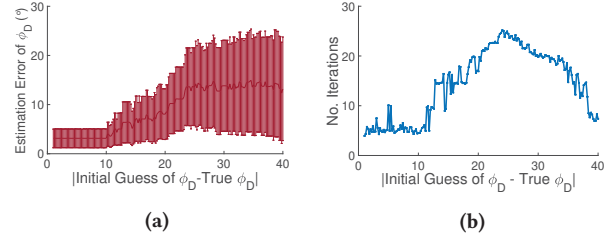


**Figure 19: Exploring the impact of initialization on (a) The estimation error and (b) The computational complexity.**

We use the same setup as shown in Fig. 8a for translation-only mobility. Fig. 19a presents LeakyTrack’s estimation error as a function of the angular distance between the initial guess and the correct LOS angle at each instance. A larger number on the x-axis means that either the translation speed is increasing (for the same  $T$ ) or  $T$  is growing (for the same mobility speed). In the latter case, the x-axis is also inversely proportional to the airtime overhead.

We observe an overall trend of higher estimation error (average and variance) when the initial guess (which is the estimate of  $\phi_D$  corresponding to the previous sample) is farther from the current RX’s angular position. Hence, it is more likely that a local minimum is achieved instead of the global minimum. Interestingly, the error is not monotonically increasing, which is due to the inherent non-linearity of the problem.

Further, we explore the number of iterations as a representation of computational complexity in Fig. 19b. We observe that an increasingly inaccurate initialization first yields more iterations. Yet ultimately, LeakyTrack would not be able to converge to the global minimum and terminates at a local minimum with fewer iterations. Hence, the reduction in computational complexity can sacrifice estimation accuracy when using a stale prior estimation. In any case, the number of iterations for exhaustive search (not shown) would be substantially higher.

*Findings: We analyzed the tradeoff between estimation accuracy, airtime overhead, and computational complexity. Increasing the tracking rate (i.e., the number of pulse transmissions per unit time) costs higher airtime overhead; yet, it offers better initialization that can yield estimation accuracy comparable to that of brute-force search, albeit with significantly less computational complexity.*

## 7 CONCLUSION

We presented LeakyTrack, a novel non-coherent and training-free system that enables nodal and environmental motion tracking with a single leaky-wave antenna. LeakyTrack correlates spatial information with spectral properties by creating unique spectral codes simultaneously in all directions. We modeled the impact of the RX’s geometric motion and a potential environmental object on the spectral profile of the received signals. We implemented the key components of LeakyTrack and demonstrated accurate estimation through extensive over-the-air experiments.

## 8 ACKNOWLEDGMENTS

We appreciate the valuable comments and feedback from the anonymous reviewers and our shepherd. This research was supported by Intel, Cisco, and by NSF grants CNS-1955075, CNS-1923782 and DOD grant W911NF1920269.

## REFERENCES

- [1] Fadel Adib, Zach Kabelac, Dina Katabi, and Robert C. Miller. 2014. 3D Tracking via Body Radio Reflections. In *Proc. USENIX NSDI*.
- [2] Fadel Adib and Dina Katabi. 2013. See through Walls with WiFi. In *Proc. ACM SIGCOMM*.
- [3] Ian F Akyildiz, Josep Miquel Jornet, and Chong Han. 2014. Terahertz Band: Next Frontier for Wireless Communications. *Physical Communication* 12 (2014), 16–32.
- [4] Ian F Akyildiz, Josep Miquel Jornet, and Chong Han. 2014. TeraNets: Ultra-Broadband Communication Networks in the Terahertz Band. *IEEE Wireless Communications* 21, 4 (2014), 130–135.
- [5] Yasith Amarasinghe, Rajind Mendis, and Daniel M. Mittleman. 2020. Real-Time Object Tracking using a Leaky THz Waveguide. *Opt. Express* 28, 12 (2020), 17997–18005.
- [6] Sheheryar Arshad, Chunhai Feng, Yonghe Liu, Yupeng Hu, Ruiyun Yu, Siwang Zhou, and Heng Li. 2017. Wi-Chase: A WiFi based Human Activity Recognition System for Sensorless Environments. In *Proc. IEEE WoWMoM*.
- [7] Constantine A Balanis and Craig R Birtcher. 2008. Antenna Measurements. *Modern Antenna Handbook* (2008), 977–1033.
- [8] Maurizio Bocca, Ossi Kalliokallio, Neal Patwari, and Suresh Venkatasubramanian. 2014. Multiple Target Tracking with RF Sensor Networks. *IEEE Transactions on Mobile Computing* 13, 8 (2014), 1787–1800.
- [9] Taiyun Chi, Min-Yu Huang, Sensen Li, and Hua Wang. 2017. 17.7 A Packaged 90-to-300GHz Transmitter and 115-to-325GHz Coherent Receiver in CMOS for Full-Band Continuous-wave mm-Wave Hyperspectral Imaging. In *Proc. of IEEE ISSCC*.
- [10] Simone Di Domenico, Mauro De Sanctis, Ernestina Cianca, Fabrizio Giuliano, and Giuseppe Bianchi. 2018. Exploring Training Options for RF Sensing Using CSI. *IEEE Communications Magazine* 56, 5 (2018), 116–123.
- [11] Irl Duling and David Zimdars. 2009. Terahertz Imaging: Revealing Hidden Defects. *Nature Photonics* 3, 11 (2009), 630.
- [12] Xiaojian Fu, Fei Yang, Chenxi Liu, Xiaojun Wu, and Tie Jun Cui. 2020. Terahertz Beam Steering Technologies: From Phased Arrays to Field-Programmable Metasurfaces. *Advanced Optical Materials* 8, 3 (2020), 1900628.
- [13] Ruipeng Gao, Yang Tian, Fan Ye, Guojie Luo, Kaigui Bian, Yizhou Wang, Tao Wang, and Xiaoming Li. 2016. Sextant: Towards Ubiquitous Indoor Localization Service by Photo-Taking of the Environment. *IEEE Transactions on Mobile Computing* 15, 2 (2016), 460–474.
- [14] Yasaman Ghasempour, Rabi Shrestha, Aaron Charous, Edward Knightly, and Daniel M. Mittleman. 2020. Single-Shot Link Discovery for Terahertz Wireless Networks. *Nature Communication* 11, 1 (2020), 2017.
- [15] Yasaman Ghasempour, Chia-Yi Yeh, Rabi Shrestha, Daniel Mittleman, and Edward Knightly. 2020. Single Shot Single Antenna Path Discovery in THz Networks. In *Proc. ACM MobiCom*.
- [16] Frank B. Gross. 2011. *Frontiers in Antennas: Next Generation Design & Engineering*. McGraw-Hill Education.
- [17] Shulabh Gupta, Samer Abielmona, and Christophe Caloz. 2009. Microwave Analog Real-Time Spectrum Analyzer (RTSA) Based on the Spectral-Spatial Decomposition Property of Leaky-Wave Structures. *IEEE Transactions on Microwave Theory and Techniques* 57, 12 (2009), 2989–2999.
- [18] Muhammad Kumail Haider, Yasaman Ghasempour, and Edward W. Knightly. 2018. Search Light: Tracking Device Mobility Using Indoor Luminaries to Adapt 60 GHz Beams. In *Proc. ACM MobiHoc*.
- [19] Daniel Headland, Yasuaki Monnai, Derek Abbott, Christophe Fumeaux, and Withawat Withayachumnankul. 2018. Tutorial: Terahertz beamforming, from concepts to realizations. *APL Photonics* 3, 5 (2018), 051101.
- [20] Nicholas J Karl, Robert W McKinney, Yasuaki Monnai, Rajind Mendis, and Daniel M Mittleman. 2015. Frequency-division Multiplexing in the Terahertz Range using a Leaky-wave Antenna. *Nature Photonics* 9, 11 (2015), 717.
- [21] Ye-Sheng Kuo, Pat Pannuto, Ko-Jen Hsiao, and Prabal Dutta. 2014. Luxapose: Indoor Positioning with Mobile Phones and Visible Light. In *Proc. ACM MobiCom*.
- [22] Heju Li, Xin He, Xukai Chen, Yinyin Fang, and Qun Fang. 2019. Wi-Motion: A Robust Human Activity Recognition Using WiFi Signals. *IEEE Access* 7 (2019), 153287–153299.
- [23] Liqun Li, Pan Hu, Chunyi Peng, Guobin Shen, and Feng Zhao. 2014. Epsilon: A Visible Light Based Positioning System. In *Proc. of USENIX NSDI*.
- [24] Jaime Lien, Nicholas Gillian, M. Emre Karagozler, Patrick Amihood, Carsten Schwesig, Erik Olson, Hakim Raja, and Ivan Poupyrev. 2016. Soli: Ubiquitous Gesture Sensing with Millimeter Wave Radar. *ACM Transactions Graphics*, Article 142 (2016).
- [25] Song Liu and Tian He. 2017. SmartLight: Light-Weight 3D Indoor Localization Using a Single LED Lamp. In *Proc. ACM Sensys (SenSys '17)*. Article 11, 14 pages.
- [26] Jianjun Ma, Nicholas J Karl, Sara Bretin, Guillaume Ducournau, and Daniel M Mittleman. 2017. Frequency-Division Multiplexer and Demultiplexer for Terahertz Wireless Links. *Nature Communications* 8, 1 (2017), 1–8.
- [27] Hironori Matsumoto, Issei Watanabe, Akifumi Kasamatsu, and Yasuaki Monnai. 2020. Integrated Terahertz Radar based on Leaky-Wave Coherence Tomography. *Nature Electronics* 3, 2 (2020), 122–129.
- [28] Kosuke Murano, Issei Watanabe, Akifumi Kasamatsu, Safumi Suzuki, Masahiro Asada, Withawat Withayachumnankul, Toshiyuki Tanaka, and Yasuaki Monnai. 2016. Low-Profile Terahertz Radar based on Broadband Leaky-Wave Beam Steering. *IEEE Transactions on Terahertz Science and Technology* 7, 1 (2016), 60–69.
- [29] Sameera Palipana, David Rojas, Piyush Agrawal, and Dirk Pesch. 2018. FallDeFi: Ubiquitous Fall Detection Using Commodity Wi-Fi Devices. *Proc. ACM Interactive Mobile Wearable Ubiquitous Technologies* 1, 4 (2018).
- [30] Hamed Rahmani, Yuxiang Sun, Mohit Kherwa, Suparno Pal, and Aydin Babakhani. 2020. Coherent Radiation from a Swarm of Wirelessly Powered and Synchronized Sensor Nodes. *IEEE Sensors Journal* (2020), 1–1.
- [31] Theodore S Rappaport, Yunchou Xing, Ojas Kanhere, Shihao Ju, Arjuna Madanayake, Soumyajit Mandal, Ahmed Alkhatieb, and Georgios C Trichopoulos. 2019. Wireless Communications and Applications above 100 GHz: Opportunities and Challenges for 6G and Beyond. *IEEE Access* 7 (2019), 78729–78757.
- [32] Moustafa Seifeldin, Ahmed Saeed, Ahmed E. Kosba, Amr El-Keyi, and Moustafa Youssef. 2013. Nuzzer: A Large-Scale Device-Free Passive Localization System for Wireless Environments. *IEEE Transactions on Mobile Computing* 12, 7 (2013), 1321–1334.
- [33] Kaushik Sengupta and Ali Hajimiri. 2012. A 0.28 THz Power-Generation and Beam-Steering Array in CMOS based on Distributed Active Radiators. *IEEE Journal of Solid-State Circuits* 47, 12 (2012), 3013–3031.
- [34] Kaushik Sengupta, Tadao Nagatsuma, and Daniel M Mittleman. 2018. Terahertz Integrated Electronic and Hybrid Electronic–Photonic Systems. *Nature Electronics* 1, 12 (2018), 622–635.
- [35] Adrian Sutinjo, Michal Okoniewski, and Ronald. H. Johnston. 2008. Radiation from Fast and Slow Traveling Waves. *IEEE Antennas and Propagation Magazine* 50, 4 (2008), 175–181.
- [36] Yuxi Wang, Kaishun Wu, and Lionel M. Ni. 2017. WiFall: Device-Free Fall Detection by Wireless Networks. *IEEE Transactions on Mobile Computing* 16, 2 (2017), 581–594.
- [37] Teng Wei and Xinyu Zhang. 2015. MTrack: High-Precision Passive Tracking Using Millimeter Wave Radios. In *Proc. ACM MobiCom*.
- [38] Bo Xie, Guang Tan, and Tian He. 2015. SpinLight: A High Accuracy and Robust Light Positioning System for Indoor Applications. In *Proc. ACM Sensys (SenSys '15)*.
- [39] Chenren Xu, Bernhard Firner, Robert S. Moore, Yanyong Zhang, Wade Trappe, Richard Howard, Feixiong Zhang, and Ning An. 2013. SCPL: Indoor Device-Free Multi-Subject Counting and Localization Using Radio Signal Strength. In *Proc. IPSN*.
- [40] Zhice Yang, Zeyu Wang, Jiansong Zhang, Chenyu Huang, and Qian Zhang. 2015. Wearables Can Afford: Light-Weight Indoor Positioning with Visible Light. In *Proc. ACM MobiSys (MobiSys '15)*.
- [41] Chia-Yi Yeh, Yasaman Ghasempour, Yasith Amarasinghe, Daniel Mittleman, and Edward Knightly. 2020. Security in Terahertz WLANs with Leaky Wave Antennas. In *Proc. ACM WiSec*.
- [42] Moustafa Youssef, Matthew Mah, and Ashok Agrawala. 2007. Challenges: Device-Free Passive Localization for Wireless Environments. In *Proc. ACM MobiCom*.
- [43] Chi Zhang and Xinyu Zhang. 2017. Pulsar: Towards Ubiquitous Visible Light Localization. In *Proc. ACM MobiCom*.